



2nd Advanced Optical Metrology Compendium

Advanced Optical Metrology

Geoscience | Corrosion | Particles | Additive Manufacturing: Metallurgy, Cut Analysis & Porosity



EVIDENT
OLYMPUS

WILEY

The latest eBook from **Advanced Optical Metrology**.
Download for free.

This compendium includes a collection of optical metrology papers, a repository of teaching materials, and instructions on how to publish scientific achievements.

With the aim of improving communication between fundamental research and industrial applications in the field of optical metrology we have collected and organized existing information and made it more accessible and useful for researchers and practitioners.

EVIDENT
OLYMPUS

WILEY

Displacive Order–Disorder Behavior and Intrinsic Clustering of Lattice Distortions in Bi-Substituted NaNbO_3

Igor Levin,* Fan Yang, Russell Maier, William J. Laws, Dean S. Keeble, Giannantonio Cibin, and Derek C. Sinclair

Perovskite-like $\text{NaNbO}_3\text{-Bi}_{1/3}\text{NbO}_3$ solid solutions are studied to understand the interactions between octahedral rotations, which dominate the structural behavior of NaNbO_3 and displacive disorder of Bi present in $\text{Bi}_{1/3}\text{NbO}_3$. Models of instantaneous structures for representative compositions are obtained by refining atomic coordinates against X-ray total scattering and extended X-ray-absorption fine structure data, with additional input obtained from transmission electron microscopy. A mixture of distinct cations and vacancies on the cuboctahedral A-sites in $\text{Na}_{1-3x}\text{Bi}_x\text{NbO}_3$ ($x \leq 0.2$) results in 3D nanoscale modulations of structural distortions. This phenomenon is determined by the inevitable correlations in the chemical composition of adjacent unit cells according to the structure type—an intrinsic property of any nonmolecular crystals. Octahedral rotations become suppressed as x increases. Out-of-phase rotations vanish for $x > 0.1$, whereas in-phase tilts persist up to $x = 0.2$, although for this composition their correlation length becomes limited to the nanoscale. The loss of out-of-phase tilting is accompanied by qualitative changes in the probability density distributions for Bi and Nb, with both species becoming disordered over loci offset from the centers of their respective oxygen cages. Symmetry arguments are used to attribute this effect to different strengths of the coupling between the cation displacements and out-of-phase versus in-phase rotations. The displacive disorder of Bi and Nb combined with nanoscale clustering of lattice distortions are primarily responsible for the anomalous broadening of the temperature dependence of the dielectric constant.

1. Introduction

Complex perovskite titanates that incorporate bismuth cations together with larger, less polarizable species on 12-fold coordi-

Dr. I. Levin, Dr. R. Maier, W. J. Laws
Materials Measurement Science Division
National Institute of Standards and Technology
Gaithersburg, MD 20899, USA
E-mail: igor.levin@nist.gov

Dr. F. Yang, Prof. D. C. Sinclair
Department of Materials Science and Engineering
University of Sheffield
Sheffield S1 3JD, UK

Dr. D. S. Keeble, Dr. G. Cibin
Diamond Synchrotron Light Source
Didcot OX11 0DE, UK

 The ORCID identification number(s) for the author(s) of this article can be found under <https://doi.org/10.1002/adfm.202001840>.

DOI: 10.1002/adfm.202001840

nated A-sites attract interest as promising dielectrics, piezoelectrics, and ion conductors.^[1–4] The relatively small Bi cations, which generally exhibit a stereochemically active lone pair of electrons,^[5] are stabilized by distortions of $[\text{BiO}_{12}]$ coordination environments via combined Bi and oxygen displacements that yield shorter, relatively covalent Bi–O bonds. The exact distortion mechanism depends on the Goldsmith perovskite tolerance factor.^[6] If Bi shares A-sites with larger cations (e.g., K, Ba), a cooperative relaxation of the oxygen framework in the form of octahedral rotations is suppressed and shorter Bi–O bonds are achieved predominantly via Bi displacements.^[7,8] In systems with Bi-companion species small enough to induce rotations (e.g., Na), both Bi and oxygen displacements contribute significantly.^[9,10] As dielectric and transport properties are strongly affected by polar Bi displacements, the ability to manipulate their behavior would facilitate materials design.

Typically, Bi is found to be offset preferentially along the $\langle 100 \rangle_c$ and/or $\langle 111 \rangle_c$ (hereafter, the subscript “c” refers to an ideal ≈ 4 Å cubic perovskite cell) directions. In many systems with disordered distributions of A-site cations, correlations among Bi displacements are limited to the nanoscale.^[7–9] In some cases, the average symmetry, as seen by Bragg diffraction, remains cubic down to low temperatures,^[7,8] while in others, phase transitions associated with cation shifts and octahedral rotations occur.^[9,10] A ferroelectric phase transition is accompanied by the ordering of Bi displacements although a significant degree of disorder can be retained well below the Curie temperature.^[7] Transitions manifested in a change of preferred directions of such disordered displacements within a polar phase have also been observed.^[7,9] However, the strength of coupling between different patterns of octahedral tilting (hereafter, “rotations” and “tilting” are used interchangeably) and Bi off-centering remains uncertain.

The most studied Bi-based titanate that combines both types of distortions is $\text{Na}_{1/2}\text{Bi}_{1/2}\text{TiO}_3$. The in-phase and out-of-phase octahedral rotations in this compound exhibit disparate correlation lengths which give rise to hierarchical nanoscale domains.^[9,11] Such complexity makes it difficult to disentangle various types of atomic displacements and their spatial correlations. Several reported studies of the local structure in this

compound have provided some insights into the behavior of Bi^{3+} but the coupling of octahedral rotations to the cation displacements has not been analyzed.

Here, we investigate the relations between octahedral tilting and Bi off-centering in $(\text{Na,Bi})\text{NbO}_3$ solid solutions. While less explored than the titanates, Bi-based alkaline niobates^[12] also offer potentially exploitable properties both on their own and as components in solid solutions. NaNbO_3 undergoes a sequence of phase transitions on cooling from the high-temperature paraelectric cubic phase to the lowest temperature ferroelectric rhombohedral structure.^[13–15] These transitions, which generate seven polymorphs, originate from competing in-phase and out-of-phase octahedral rotations combined with off-center cation (Na, Nb) displacements. Several NaNbO_3 polymorphs, including the room-temperature form, exhibit complex rotations of $[\text{NbO}_6]$ octahedra which result in orthorhombic superstructures with quadrupled or sextupled periodicities along one of the cubic axes. Substitution of Bi^{3+} , which in 12-fold coordination is projected to have a slightly smaller radius ($R = 1.35 \text{ \AA}$)^[16] than Na^+ ($R = 1.39 \text{ \AA}$), reduces the overall tolerance factor and as such can be expected to promote octahedral tilting. However, the presence of A-site vacancies required to compensate for the extra positive charge introduced by Bi^{3+} can disrupt correlations among oxygen displacements. Likewise, the off-centering of Bi ions can counter the enhanced driving force for tilting.

We considered compositions along the $\text{NaNbO}_3\text{-Bi}_{1/3}\text{NbO}_3$ join in the mostly unstudied ternary $\text{Na}_2\text{O-Nb}_2\text{O}_5\text{-Bi}_2\text{O}_3$ system. $\text{Bi}_{1/3}\text{NbO}_3$ has been obtained previously as a metastable phase upon cooling a liquid.^[17] Single-crystal X-ray diffraction (XRD) confirmed its structure to be tetragonal ($P4/mmm$) symmetry with an $a \times a \times 2a$ unit cell ($a \approx 4 \text{ \AA}$).^[17] This doubling of the ideal perovskite cell reflects partial ordering of Bi atoms and A-site vacancies which segregate into alternate (001) planes with Bi occupancies of 28% and 42%, respectively. Bi atoms are displaced $\approx 0.4 \text{ \AA}$ from the high-symmetry $4/mmm$ positions, disordered among the eight split sites offset approximately along the $\langle 111 \rangle$ cubic directions. Thus, $\text{Na}_{1-3x}\text{Bi}_x\text{NbO}_3$ solid solutions provide a suitable if still relatively complex system for studying the interrelation between octahedral rotations, which are prominent in NaNbO_3 , and the disordered Bi displacements that exist in $\text{Bi}_{1/3}\text{NbO}_3$.

Our results demonstrate that in the presence of chemical disorder, the perovskite topology necessarily results in nanoscale clustering of lattice distortions which occur to accommodate the competing bonding requirements of constituent species. A-site vacancies inhibit octahedral tilting and the disappearance of out-of-phase rotations promotes the displacive disorder of Bi and Nb. We propose that this order/disorder transition, combined with the heterogeneous lattice distortions, results in the marked flattening of the temperature dependence of the dielectric constant.

2. Experimental Section

$\text{Na}_{1-3x}\text{Bi}_x\text{NbO}_3$ ($x = 0, 0.1, 0.15, 0.2$) samples (5 g) were prepared using solid-state synthesis starting from powders of Na_2CO_3 (A.R.), Bi_2O_3 (99.999%), and Nb_2O_5 (99.999%). Prior to

weighing, Na_2CO_3 was dried at $180 \text{ }^\circ\text{C}$. The powders were mixed by grinding under acetone using an agate mortar and pestle. Mixtures were ball-milled in isopropanol in a planetary mill for 30 min with yttria-stabilized zirconia cylinders as the grinding media. The dried powders were calcined at $850 \text{ }^\circ\text{C}$ in an alumina crucible. After a second ball milling, samples were pressed into pellets and heated in air at temperatures between 1000 and $1200 \text{ }^\circ\text{C}$ for 5 h followed by quenching in air. Laboratory XRD with $\text{Cu K}\alpha_1$ radiation was used to confirm phase purity.

X-ray total-scattering data were collected at the I-15-A (Diamond Light Source, UK) beamline. The measurements were performed at room temperature using an incident beam energy of 76.7 keV with a 2D detector positioned 235 mm downstream from the sample. The samples were loaded in 0.4 mm quartz capillaries, mounted on a sample changer, and spun during measurements. The instrumental resolution function was determined by measuring NIST Si SRM 640c. The as-collected 2D X-ray data were reduced using the DAWN software package^[18] and then converted to the total-scattering function and $G(r)$ using PDFGetX3.^[19] Extended X-ray absorption fine structure (EXAFS) measurements were performed for the Bi L_3 -edge at the B18 beamline of the Diamond Light Source, with the data collected in transmission. The EXAFS data were reduced using the Athena software package;^[20] preliminary analysis of these data was performed in Artemis.^[20] The scattering amplitudes and phases were calculated using FEFF8.^[21] Transmission electron microscopy (TEM) studies were conducted on selected samples using two different conventional instruments operated at 200 and 300 kV, respectively. Samples for transmission TEM were prepared using either mechanical polishing followed by ion thinning at $T = -100 \text{ }^\circ\text{C}$ until perforation, or by dispersing a suspension of the crushed powder in ethanol on a lacey-carbon-coated grid. The latter method was used to ensure the observed structural features were not artifacts of the ion-thinning procedure.

Rietveld average-structure refinements and symmetry-constrained small-box X-ray fits of a pair-distribution function (PDF) were performed in the academic version of the TOPAS software (version 6).^[22,23] Atomistic structure refinements were carried out in the RMCProfile software.^[24–25] The structure was modeled using atomic configurations which contained $36 \times 36 \times 36$ unit cells (or equivalent for noncubic cases) with 233 280 atoms, sampling interatomic distances up to 7 nm. The distributions of Bi, Na, and A-site vacancies for each composition were assumed per the TEM data, which provided direct information on the type and spatial extent of short-range chemical ordering, where present, as discussed in the results section; besides providing real-space imaging capabilities, TEM is more sensitive to short-range order than X-rays because of much stronger interactions of electrons with the matter. The atomic coordinates were varied according to the RMC algorithm to simultaneously fit the X-ray total-scattering signal and its real-space Fourier transform, which represents a PDF. The Bi EXAFS data were also included in the fit to constrain the nearest-neighbor Bi–O and Bi–Nb distances. Additionally, polyhedral restraints were imposed on the $[\text{NbO}_6]$ octahedra to regularize the refined configuration. The reciprocal- and real-space forms of the X-ray scattering data were corrected for instrument resolution.^[26] The weights assigned to the individual datasets were adjusted automatically during fits according to an algorithm that

Table 1. Interatomic pair contributions (in fractions) to X-ray total scattering in $\text{Na}_{1-3x}\text{Bi}_x\text{NbO}_3$ calculated assuming fixed scattering factors equal to the respective elemental atomic numbers. Values ≥ 0.1 are highlighted in bold. In practice, the RMCProfile software accounts for the Q -dependence of the atomic scattering factors.

x	Na–Na	Na–Bi	Na–Nb	Na–O	Bi–Bi	Bi–Nb	Bi–O	Nb–Nb	Nb–O	O–O
0	0.02	–	0.156	0.09	–	–	–	0.29	0.34	0.10
0.1	0.009	0.014	0.097	0.06	0.010	0.10	0.06	0.26	0.30	0.09
0.2	0.003	0.02	0.049	0.029	0.037	0.18	0.108	0.227	0.27	0.08

employs a statistical analysis to ensure that each residual term decreases over time to a small preset value. The resulting atomistic models represent instantaneous structure.

For $(\text{Na,Bi})\text{NbO}_3$, X-ray total-scattering is dominated by contributions of atomic pairs that involve Nb atoms (Table 1). Thus, positions of the lighter (Na, O) or dilute (Bi) species are determined via the Na–Nb, Bi–Nb, and O–Nb separations. Including the Bi EXAFS in the fit constrains the nearest-neighbor Bi–O distances and is required for separating Bi and Na.

Variable-temperature measurements of capacitance and dielectric loss were performed on sintered pellets using an inductance capacitance resistance (LCR) meter in the frequency range between 10 and 10^5 Hz. The pellet surfaces were polished using a 9 μm diamond film and sputtered with platinum electrodes (100 μm thick). Samples were placed in a spring-loaded fixture inside a controlled-temperature chamber; the sample cooling rate was 2 $^\circ\text{C min}^{-1}$ and all data were corrected for sample geometry. Variable-temperature impedance spectroscopy on ceramics was performed with a similar arrangement using an Agilent E4980A impedance analyzer to cover the frequency range 20 Hz to 1 MHz. All data were corrected for sample geometry and analyzed using Z-view software (Scribner Associates, Inc. Southern Pines, NC).

3. Results

3.1. General Overview from X-Ray and Electron Diffraction

The substitution of Bi^{3+} for Na^+ according to the formula $\text{Na}_{1-3x}\text{Bi}_x\text{NbO}_3$ yields a single perovskite phase for $x \leq 0.2$ (Figure 1, Figure S1, Supporting Information). For $x = 0.1$ and $0.1 < x \leq 0.2$, all the Bragg peaks in the XRD patterns can be described by the orthorhombic $\sqrt{2}a \times \sqrt{2}a \times 2a$ and tetragonal $\sqrt{2}a \times \sqrt{2}a \times a$ unit cells, respectively. Metrically, the $x = 0.2$ structure appears as cubic. No attempts were made to determine a solubility range for Bi as a function of temperature. The effective cubic-perovskite unit-cell volume expands linearly as x increases (Figure S2, Supporting Information). Detailed structural characterization was performed on $x = 0.1$ and 0.2 which exhibit distinct types of octahedral tilting.

XRD patterns of $x = 0.1$ (Figure 1) contain superlattice reflections that point to the coexistence of in-phase and out-of-phase octahedral rotations ($a^-a^-c^+$ in Glazer's notation^[27]) yielding a $\sqrt{2}a \times \sqrt{2}a \times 2a$ unit cell and $Pbnm$ symmetry. Rietveld refinements supported this assignment. The $Pbnm$ model also provided a satisfactory match to the PDF (Figure S3, Supporting Information), apart from significant discrepancies in the local r -range which can be ascribed to the expectedly distinct local

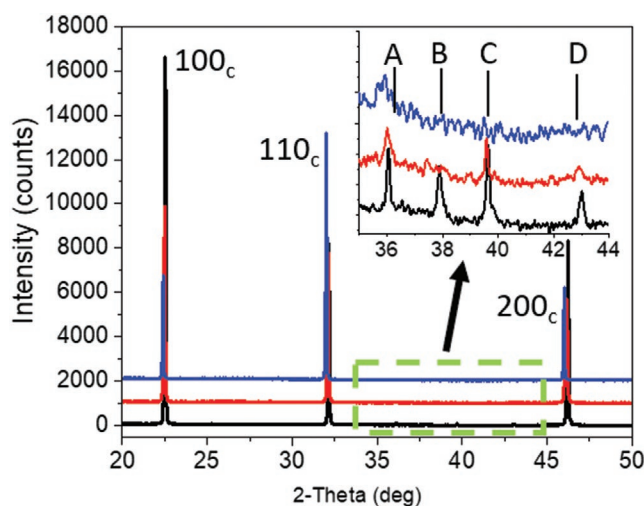


Figure 1. Portions of X-ray diffraction patterns which include superlattice reflections associated with octahedral rotations for a series of $\text{Na}_{1-3x}\text{Bi}_x\text{NbO}_3$ compositions: $x = 0.1$ (black), $x = 0.15$ (red), $x = 0.2$ (blue). A magnified view of the region outlined by the dashed green rectangle shows the superlattice reflections: A $\frac{1}{2}310_c = 120_o/210_o$ (superscripts “c” and “o” refer to the cubic $a \approx 4 \text{ \AA}$ and orthorhombic unit cells, respectively), B $\frac{1}{2}311_c = 103_o/121_o$, C $111_c = 022_o$, and D $\frac{1}{2}312_c = 122_o/212_o$. Reflections A and D are associated with in-phase tilting whereas reflection B is caused by out-of-phase rotations. Reflection C is fundamental for a perovskite lattice. As shown, long-range out-of-phase tilting is present for $x = 0.1$ but disappears for larger x -values; in-phase tilting is retained up to $x = 0.2$.

coordination of Na and Bi. Electron diffraction (Figure 2) confirmed the presence of superlattice reflections associated with $a^-a^-c^+$ tilting at $\frac{1}{2}zhk0$ ($h, k = \text{odd}$), $\frac{1}{2}hkl$ ($h, k, l = \text{odd}$), and $\frac{1}{2}zhk0$ ($h = \text{even}, k = \text{odd}$). However, reflection conditions expected for the n -glide symmetry planes were relaxed suggesting that the actual symmetry is $Pb2_1m$, as in the ferroelectric Q -phase of NaNbO_3 , or lower. The diffraction patterns from many crystallites contained incommensurate spots described by a modulation vector $\mathbf{q} = 1/(6 + \delta)[100]^*_c$ ($\delta \approx 0.1$; asterisk indicates reciprocal space), which is parallel to one of the $\langle 100 \rangle_c$ directions associated with the out-of-phase rotations in the $a^-a^-c^+$ structure (Figure 2d). Dark-field imaging using these reflections highlighted a fine-striation contrast (Figure 2), attributable to defects in the sequence of out-of-phase tilts. A sixfold periodicity exists in the high-temperature R polymorph of NaNbO_3 ^[28] and several possible sequences of clockwise/zero/anticlockwise rotations that could account for this superlattice have been proposed. Similar sequences or combinations thereof are likely to underlie the incommensurate $x = 0.1$

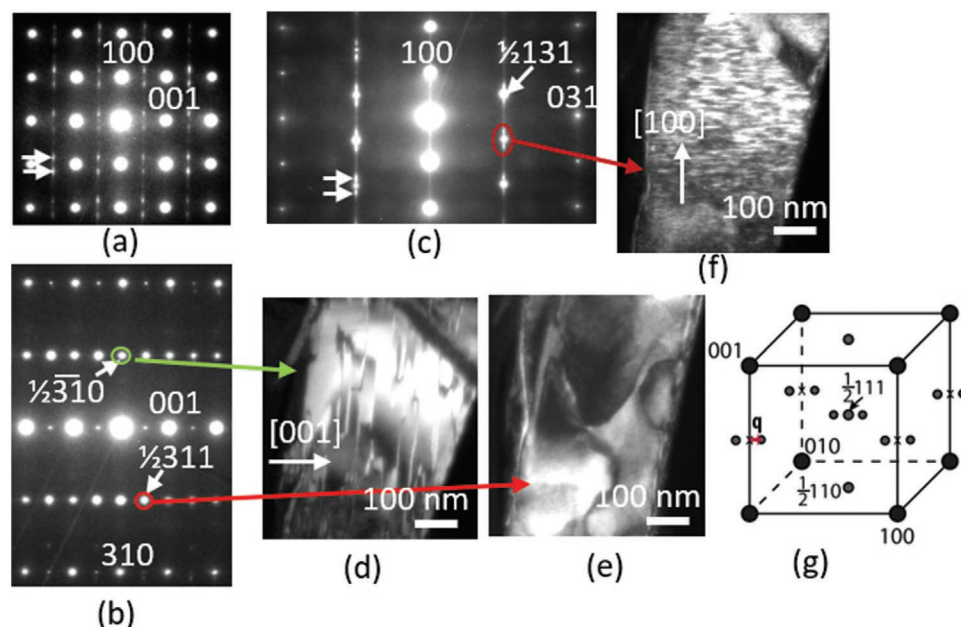


Figure 2. a–c) Representative selected area electron diffraction patterns and d–f) dark field TEM images recorded from the same crystallite for $x = 0.1$. The reflections are indexed according to a cubic perovskite unit cell with $a \approx 4 \text{ \AA}$. The $\frac{1}{2}310_c$ - and $\frac{1}{2}311_c$ -type reflections in (b) are indicative of in-phase and out-of-phase octahedral rotations, respectively. d, e) Dark field images recorded with these reflections strongly excited near the $[-130]_c$ zone-axis orientation (shown in b) highlight antiphase domains associated with each type of tilting. d) For in-phase tilts, the domain boundaries are faceted on the $\{100\}_c$ planes normal to the tilting axis. In contrast, e) the domain boundaries associated with the out-of-phase tilts are curved. The incommensurate spots visible in (a, c) are marked with white arrows. The modulation vector is $\mathbf{q} = 1/(6 + \delta)[100]_c \times (\delta \approx 0.1)$. f) A dark field image recorded with these reflections displays fine striations perpendicular to the modulation direction, which are attributed to faults in the sequence of out-of-phase tilting as discussed in the text. g) A schematic drawing of the reciprocal lattice reconstructed from a series of electron diffraction patterns. The incommensurate modulation vector \mathbf{q} is parallel to one of the cubic axes about which the octahedra rotate out of phase. Crosses mark locations of the $\frac{1}{2}h0_l$ ($h = 2n, l = 2n + 1$) reflections which would be observed in $a^-a^-c^+$ structure without modulation. $\langle 100 \rangle$ diffraction patterns from certain areas (Figure S4, Supporting Information) exhibit weak but sharp peaks at these locations suggesting that the sample is a mixture of the commensurate and modulated structures.

structure. The tilting modulation can be accompanied by a modulation of the cation displacements. Some grains exhibited coexistence of the commensurate $a^-a^-c^+$ -tilted and incommensurately modulated structures (Figure S4, Supporting Information), each possibly favored by slightly different Na/Bi ratios. In all cases, the diffraction patterns featured traces of $\langle 001 \rangle_c$ diffuse-scattering sheets which are commonly attributed to correlated Nb displacements along the octahedral chains. Despite a relatively significant concentration of the A-site vacancies (0.2), no evidence of their ordering could be observed.

For $x = 0.2$, in the XRD patterns, only a broad superlattice peak $\frac{1}{2}hk0$ ($h, k = \text{odd}$) attributed to in-phase tilting could be detected (Figure 1), whereas electron diffraction (Figure 3) revealed sharp spots at both $\frac{1}{2}hk0$ ($h, k = \text{odd}$) and $\frac{1}{2}hkl$ ($h, k, l = \text{odd}$) locations. Analysis of a series of crystal orientations demonstrated that these spots represent intersections of continuous rods of diffuse intensity with the relevant reciprocal-lattice sections, as illustrated using a schematic drawing in Figure 3. Such diffuse $\langle 100 \rangle$ rods are typical for disordered clockwise/anticlockwise octahedral rotations about a corresponding cubic axis. The diffuse intensity distributions along the rods as seen in the $\langle 310 \rangle_c$ patterns exhibit visible condensation of intensity at the $\frac{1}{2}hk0$ ($h, k = \text{odd}$) locations, which suggests short-range ordering of the in-phase tilts, in accord with the XRD results (Figure 1). The out-of-phase rotations result from planar defects in the otherwise in-phase tilting sequence, such

as ...+++---++---+++..., etc. Dark-field images recorded using the $\frac{1}{2}310$ reflection in both $\langle 310 \rangle_c$ and $\langle 331 \rangle_c$ orientations highlight nanoscale domains associated with the presumed octahedral rotations (Figure 3); the sizes of these domains are consistent with broadening of the superlattice peak observed by XRD. The diffraction patterns also contain diffuse maxima at $\frac{1}{2}hk0$ ($h = \text{even}, k = \text{odd}$) which are a signature of short-range ordering for Na, Bi, and A-site vacancies. This ordering results in alternating $\{100\}_c$ layers having distinct A-site compositions (e.g., vacancy-rich and vacancy-poor), as in $\text{Bi}_{1/3}\text{NbO}_3$. Other diffuse-scattering features included the $\{100\}_c$ sheets associated with correlated cation displacements and strongly asymmetric diffuse intensity near the Bragg reflections, which is likely caused by lattice distortions in response to the chemical disorder.

3.2. Local Structure from RMC Refinements

Following the TEM results, models for the $x = 0.1$ structure assumed a random distribution of Na, Bi, and vacancies over the A-sites. The starting configuration incorporated both in-phase and out-of-phase octahedral rotations ($a^-a^-c^+$) as per Rietveld refinements; the incommensurate modulation was ignored because in the present case it is unlikely to significantly affect the local structure as the model accounts for the

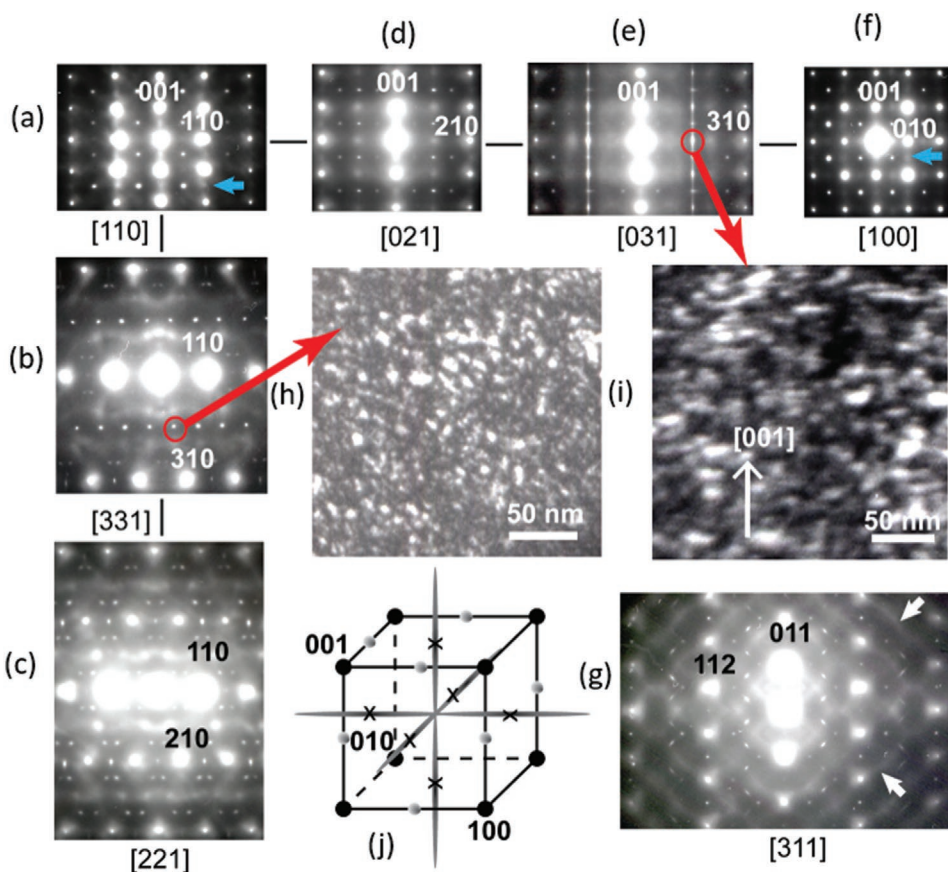


Figure 3. a–g) A series of representative selected area electron diffraction patterns recorded from the same grain of $x = 0.2$. The reflections are indexed according to a cubic perovskite unit cell with $a \approx 4 \text{ \AA}$. Relatively sharp superlattice spots are present at $\frac{1}{2}hk0$ ($h = 2n, k = 2n$) and $\frac{1}{2}hkl$ ($h = 2n + 1, k = 2n + 1, l = 2n + 1$). The spots at $\frac{1}{2}hkl$ ($h = 2n + 1, k = 2n + 1, l = 2n + 1$) appear to result from the intersection of diffuse rods of intensity with the reciprocal-lattice sections (e.g., [331], [221]) captured in the diffraction patterns. The presence of diffuse rods reflects disordered octahedral rotations about a given cubic axis. The condensation of diffuse intensity at $\frac{1}{2}hk0$ ($h = 2n, k = 2n$) locations indicates a preference for in-phase tilting. h, i) Dark field images recorded with the same $\frac{1}{2}310$ reflections but near the two different zone-axis orientations (i.e., [331] and [031]) highlight a correlation length of $\approx 10 \text{ nm}$ for in-phase rotations. j) A schematic drawing of the reciprocal lattice illustrating the diffuse-scattering rods and their intersections.

overall character of the tilting distortion. For $x = 0.2$, two types of A-species distributions were considered. In the first case, the starting configuration was an assemblage of three nanodomain variants, 2 nm in size, each with a layered arrangement of the A-site species represented by the ordering vectors $\mathbf{k}_1 = \frac{1}{2} [100]^*_c$, $\mathbf{k}_2 = \frac{1}{2} [010]^*_c$, $\mathbf{k}_3 = \frac{1}{2} [001]^*_c$, respectively. In each variant, the alternating $\{001\}$ layers of A-cations were assumed to have the following compositions: $A1 = \text{Na}_{0.6}\text{Bi}_{0.4}$ and $A2 = \text{Na}_{0.2}\square_{0.8}$ (hereafter, the symbol \square indicates A-site vacancies). The distributions of species within these layers were random. Volume fractions of the three variants were approximately equal so that the overall symmetry was cubic. The fraction of atoms in the ordered regions was ≈ 0.75 . This starting model conforms to the TEM observations. In the second case, a random distribution of Na, Bi, and vacancies was assumed. The distributions of the A-site species were kept fixed during the refinements and only the atomic coordinates were varied. The structural characteristics considered in this study exhibited qualitatively similar trends regardless of the assumed A-site occupancy distributions; the results for $x = 0.2$ presented below correspond to the more realistic model with ordered nanodomains.

For both compositions, satisfactory fitting quality was obtained for all datasets (Figure 4). For $x = 0.1$, the coordinates of the inequivalent Wyckoff positions in the average structure were determined by folding the refined configuration onto the $\sqrt{2}a \times \sqrt{2}a \times 2a$ unit cell according to $Pb2_1m$ symmetry. The positions of Na and Bi were found to be distinct. Na is displaced by $\approx 0.1 \text{ \AA}$ predominantly along the orthorhombic γ -axis parallel to the $[110]_c$ direction, whereas Bi is additionally offset relative to Na by $\approx 0.1 \text{ \AA}$ along the $\langle 100 \rangle_c$ directions in the orthorhombic c -plane. The atomic probability density distributions (PDD) of both Na and Bi are anisotropic with a certain preference for $[001]_o$ displacements (Figure 5); the symmetry of these PDDs is consistent with the site symmetry ($\cdot m$) of the A-cation positions in the $Pb2_1m$ structure. The bond valence sum (BVS)^[29] for Bi is ≈ 2.65 , which is significantly smaller than the ideal value of 3.0; however, such underbonding is not unusual for Bi residing in relatively large oxygen cages. The BVS values for other species are nearly ideal. The PDD for Nb is nearly Gaussian but anisotropic with larger magnitudes of displacements in the a - b plane. This result is consistent with existing data for the structures of orthorhombic NaNbO_3 ^[30] and KNbO_3 ^[31] which

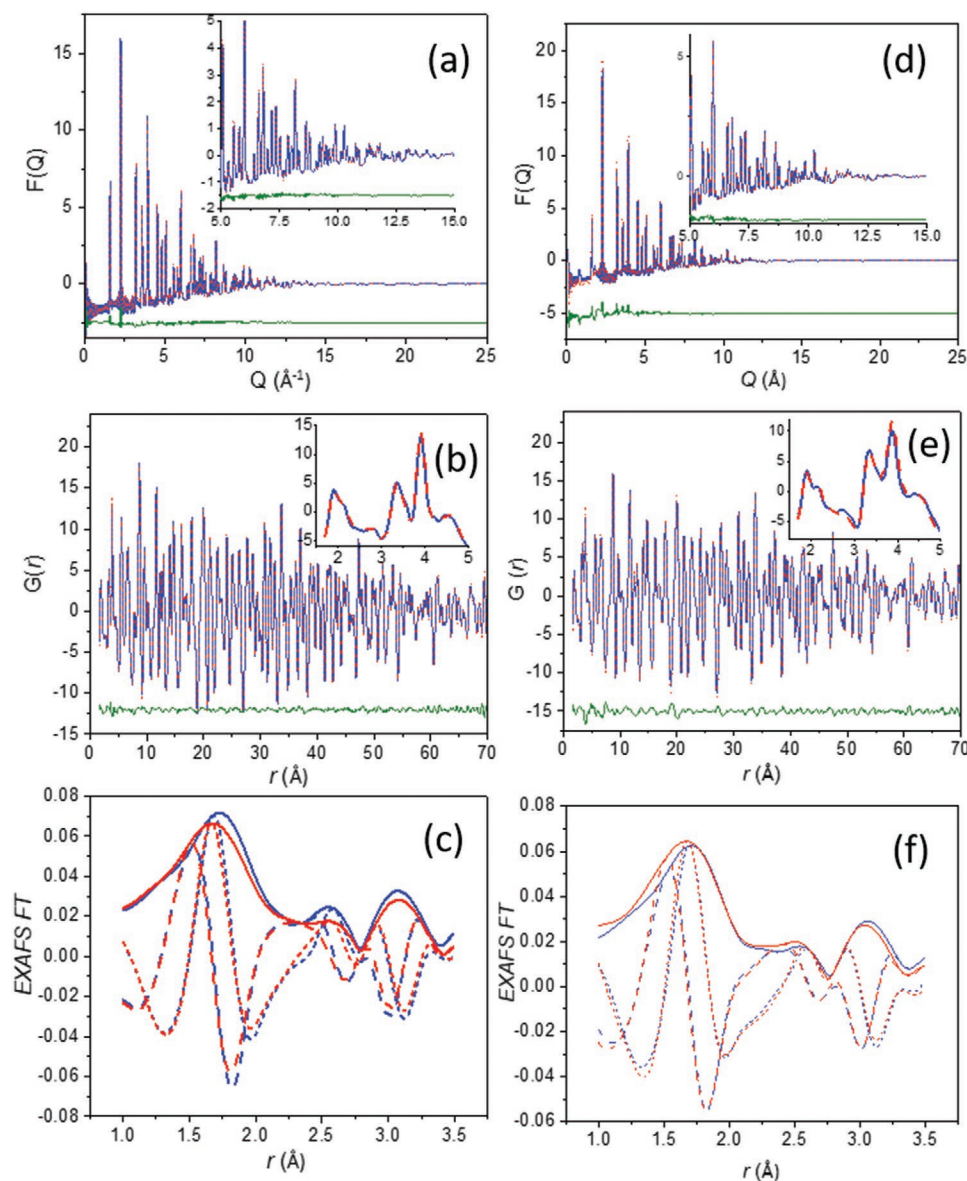


Figure 4. Experimental (red) and calculated (blue) X-ray total-scattering and Bi EXAFS data for specimens of a–c) $x = 0.1$ and d–f) 0.2 . a, d) $F(Q)$, b, e) $G(r)$, c, f) Bi EXAFS. The residual traces are shown in green. For $F(Q)$ and $G(r)$, the insets display magnified views of the mid- Q and low- r regions, respectively. For the EXAFS data, the magnitude (solid) as well as the real (dotted) and imaginary (dashed) parts of the Fourier transform (FT) are shown. The k -range of the EXAFS data used in the FT was from 2.5 to 11.6 \AA^{-1} ; prior to the FT, the k -space data was multiplied by k . The calculated signals correspond to atomic configurations refined using the RMC method simultaneously against all three datasets.

indicate that the magnitudes of the locally correlated components of Nb displacements in the c -direction that give rise to the (001) diffuse sheets are relatively small. Sectioning the Nb PDD indicates that the maximum probability is near the average position.

For $x = 0.2$, the configurations were reduced to a single cubic perovskite cell according to $Pm\bar{3}m$ symmetry. In contrast to $x = 0.1$, the PDD of Bi resembles a hollow octahedron (Figure 6). The six sites offset from the ideal cubic position by $\approx 0.37 \text{ \AA}$ along the $\langle 100 \rangle_c$ directions are preferred (Figure 6d), which are in contrast to the $\langle 111 \rangle$ displacements reported for $\text{Bi}_{1/3}\text{NbO}_3$. The average BVS for Bi remains at ≈ 2.65 . The Na displacements are considerably smaller compared to those of

Bi, and the Na PDD (not shown) appears as unimodal if still non-Gaussian with some preference for the $\langle 100 \rangle$ directions. Unlike in $x = 0.1$, Nb acquires a hollow PDD (Figure 7) with the maximum probability at a locus offset from the ideal average position (Figure 7, Figure S5, Supporting Information); no preferred directions for the Nb displacements could be identified. Analysis of the refined oxygen coordinates confirmed the presence of predominantly in-phase octahedral rotations ordered over the nanoscale, in agreement with the TEM data (Figure 8).

While the Na–O and Bi–O distances calculated for the average-structure model are relatively similar, their distributions in the RMC-refined configurations differ markedly (Figure 9). As expected, the $[\text{BiO}_{12}]$ coordination environment is

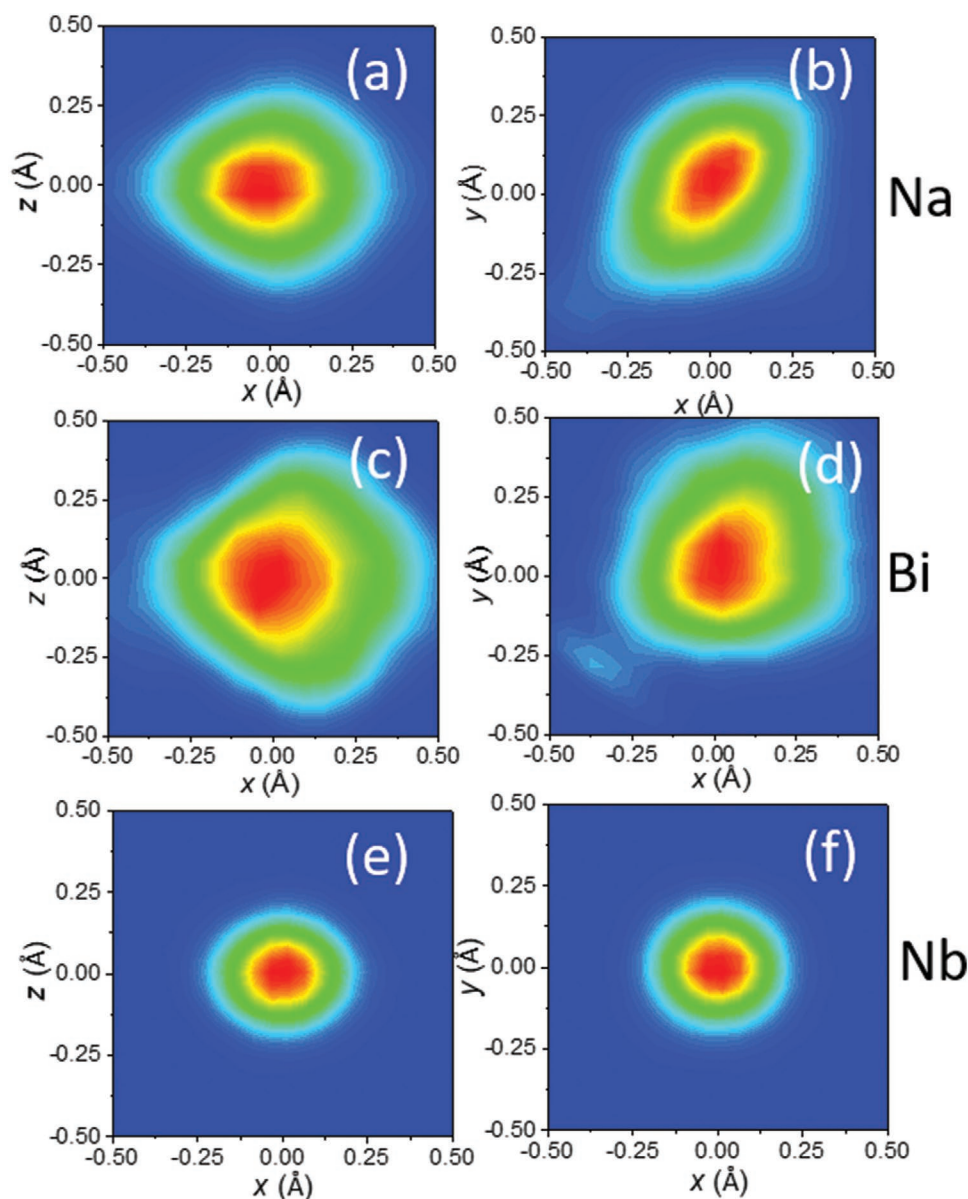


Figure 5. Projected probability density distributions (PDD for a,b) Na, c,d) Bi, and e,f) Nb in $x=0.1$. Zero coordinates in each case correspond to the average positions for each species. These PDDs were obtained by transforming the displacements of each atom of a given species in the configuration to the same inequivalent position in the $\sqrt{2}a \times \sqrt{2}a \times 2a$ unit cell according to $Pb2_1m$ symmetry. Slicing these PDDs perpendicular to the c -axis confirmed that the maximum probability occurs near the average positions. Blue and red colors denote the lowest and highest probabilities, respectively.

significantly more distorted than that of $[\text{NaO}_{12}]$, with shortest Bi–O distances of ≈ 2.2 Å, as commonly encountered in Bi-based perovskites. For comparison, for $x=0.1$, the shortest A–O distance in the average model is ≈ 2.4 Å. The individual near-neighbor Bi–O distances appear as sharp peaks, suggesting strong correlations among the Bi and O displacements, which point to a directional, covalent nature of the Bi–O bonds. In contrast, for the Na–O distribution, individual distance peaks are much broader and poorly resolved. The differences between the A–O distances as seen in the partial PDFs and those calculated from the average coordinates are largely caused by the oxygen displacements which vary strongly with the A-site coordination. Figure S6 in the Supporting Information illustrates

this effect by providing examples of projected PDDs for the oxygen atoms with none and two Bi atoms in their first coordination shell. The qualitative difference between the Na–O and Bi–O distance distributions is maintained for both compositions (Figure 9).

The local A-site chemistry affects octahedral volumes and structural distortions. Even for a random distribution of A-site species, the composition of any single unit cell is partly determined by those of its neighbors because adjacent cells share elements according to the topology of the crystal structure. For example, in the perovskite lattice, one Bi cation on a single A-site is shared by eight unit cells centered on Nb. Here, we consider clusters $[\text{Nb}_n\text{Bi}_m\text{Na}_{8-n-m}]$ which represent the A-site

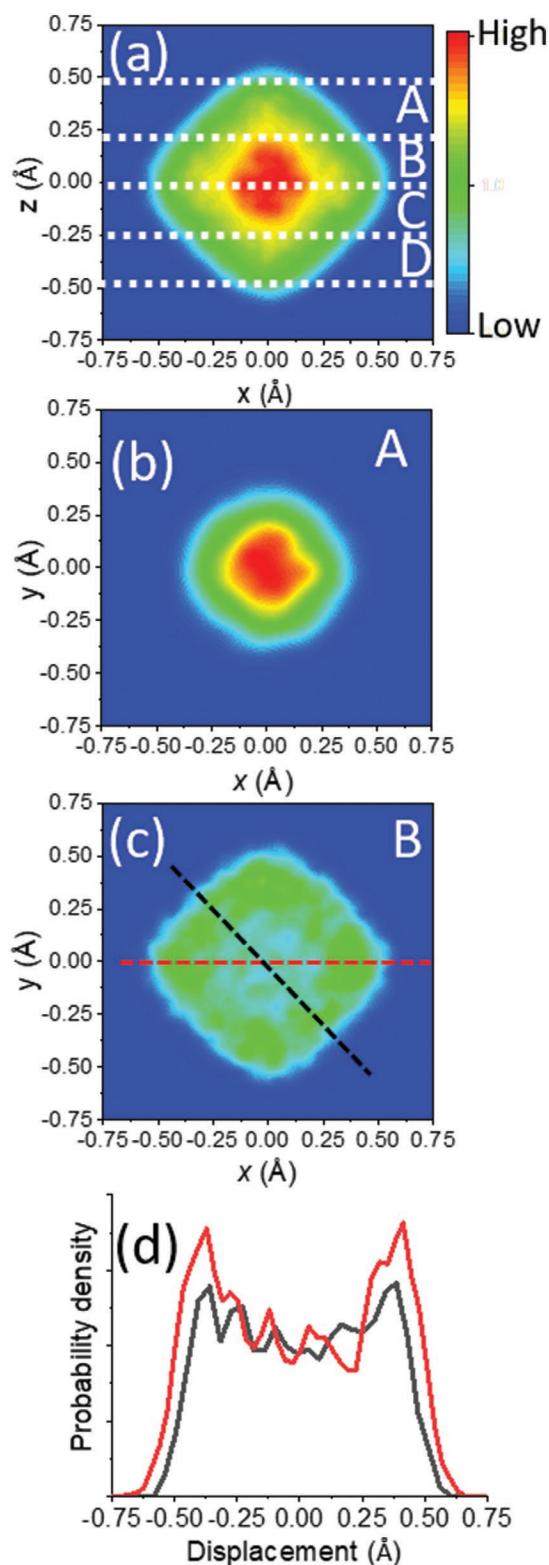


Figure 6. a) Projected probability density distribution for Bi in $x = 0.2$. b,c) Slices A and B, each 0.25 \AA thick, of this distribution perpendicular to the z -direction, as shown in (a). Zero coordinates correspond to the average positions of Bi in the cubic perovskite cell. Slices C and D (not shown) are similar to B and A, respectively. d) Values of the probability density in slice B along the dashed horizontal (red) and inclined (black)

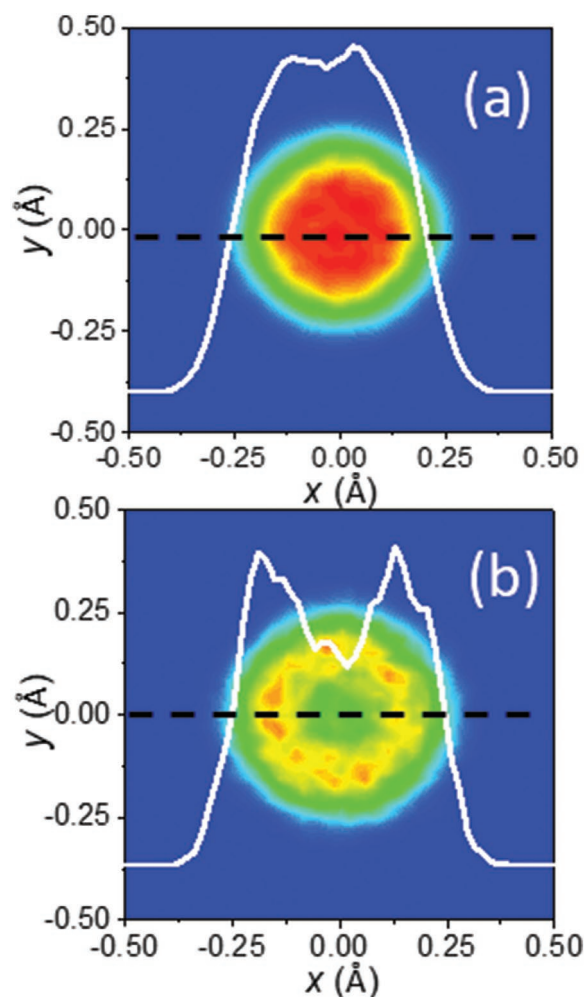


Figure 7. a) Projected probability density distribution (PDD) for Nb in $x = 0.2$. b) A slice, 0.1 \AA thick, through the center of this distribution. Zero coordinates correspond to the average position of Nb in the cubic perovskite cell. The maximum probability corresponds to a shell offset from the ideal cubic position by $\approx 0.14 \text{ \AA}$. The white line-traces represent profiles of the probability density along the horizontal dashed lines.

species fully or partially present in each perovskite unit cell. As shown in **Figure 10**, which displays color maps of n for slices of the atomic configurations, a clear preference exists for adjacent clusters to exhibit similar n -values. Moreover, clusters with $n = n$ are preferentially surrounded by those with $n = n \pm 1$, which results in 3D nanoscale modulations of composition. A similar effect exists for maps of m (not shown). The average Nb–O distances (and volumes) calculated for the individual octahedra shrink as the number of vacancies, n , in the $[\text{Nb}_{1-n}\text{Bi}_m\text{Na}_{8-n-m}]$ clusters increases (**Figure 11**). The opposite and much stronger trend occurs as a function of the local Bi content, m . Thus, as

dashed A lines are indicated in (c). A preference for the $\langle 100 \rangle$ off-centering and the minimum probability density for the average (central) position are evident. The color scale for the slices b) A and c) B is the same but different from the scale for the overall PDD in (a). Blue and red colors denote the lowest and highest probability, respectively.

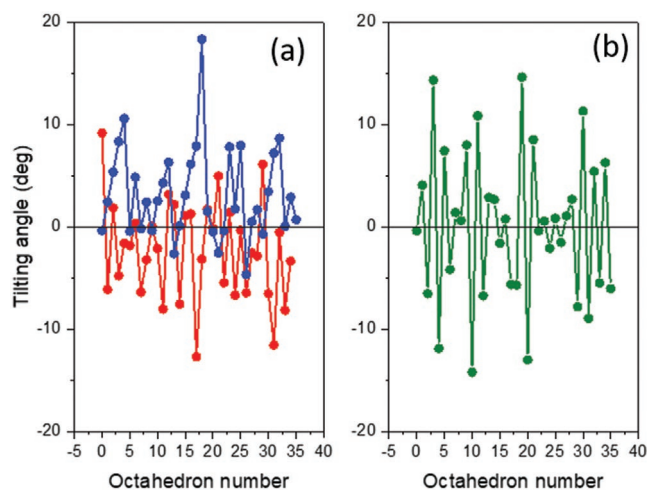


Figure 8. a) Angle of octahedral rotation about the c -axis in a refined configuration for $x = 0.2$ as a function of the octahedron number along the rotation axis for two neighboring chains (red and blue, respectively) linked via octahedral vertices. For each chain, a preference for in-phase rotations of successive octahedra is evident. As expected for rigid-unit rotations, the octahedra in two adjacent chains rotate in opposite directions. b) Angle of octahedral rotation about the c -axis as a function of the octahedron number along a chain parallel to the a -axis. The sign of rotation for successive octahedra alternates and there is a clear preference for the respective rotation angles to have similar magnitudes, again consistent with rigid-unit rotations. Similar trends were observed for rotations about the two other cubic axes. The starting configuration used in these fits exhibited no tilts. The lines are guides to the eye.

seen in Figures 10 and 11, the material exhibits a nanoscale modulation of octahedral volumes. For both compositions, the rotation angle decreases linearly as a function of n while the dependence on m , like the trends for the octahedral volumes, is reversed (Figure 12). Because each A-cation affects eight octahedra, even single-percent levels of A-site doping can have marked effects on structural distortions and the resulting properties.

The contraction of octahedral volumes for larger n can be attributed to progressive underbonding of the O atoms which is mitigated by oxygen shifts toward Nb. The observed negative correlation between the behavior of the octahedral volumes

and rotation angles can be expected for geometric reasons. The magnitude of the Nb off-centering increases linearly with m , while the dependence on n is less prominent (Figure 13). The expansion of octahedral volumes and the enhancement of the B-cation off-centering as the local concentration of Bi increases is reminiscent of the behavior observed in other systems with strongly off-centered A-cations, e.g., $(\text{Ba,Ca})\text{TiO}_3$.^[32] The Nb and A-cation (both Bi and Na) displacements are strongly and positively correlated. Likewise, strong positive correlations exist between the displacements of Nb and nearest-neighbor O atoms. For $x = 0.1$, the Nb–Nb correlations along the $\langle 100 \rangle$ directions are positive. In contrast, for $x = 0.2$, the sign of these correlations alternates for the first, second, and third nearest neighbors, which can be attributed to nanoscale ordering of the A-site vacancies since Nb cations are expected to shift toward vacancy-rich layers.

Instabilities in octahedral tilting are driven by competing A–O and B–O bonding requirements. For A-site deficient compositions, the role of the B–O bonding is expected to grow as the fraction of vacancies increases; yet, the exact effects of vacant A-sites and the nature of the B-cations on octahedral rotations have not been established.^[33] For example, perovskites that have all A-sites unoccupied exist both with (e.g., WO_3 ^[34]) and without (e.g., ReO_3 ^[35]) tilting. Our results suggest that Bi and A-site vacancies promote and suppress octahedral tilting, respectively. The net effect of these conflicting trends on the average structure is expected to depend on the A^{3+}/\square ratio. For example, in the well-studied $\text{SrTiO}_3\text{-La}_{2/3}\text{TiO}_3$ solid solutions, this ratio is 2:1 (as opposed to 1:2 in $\text{Na}_{1-3x}\text{Bi}_x\text{NbO}_3$) and therefore the tilting, on average, becomes enhanced as the fraction of $\text{La}_{2/3}\text{TiO}_3$ increases.^[36]

We characterized an effective size of the A-site $[\text{O}_{12}]$ cuboctahedral cages by considering the maximum radius of a sphere that has all 12 oxygen atoms located either on or outside its surface. For $x = 0.1$, the mean value of such a radius for the Bi sites ($\approx 2.43 \text{ \AA}$) is significantly smaller than that for the Na sites ($\approx 2.50 \text{ \AA}$), with the vacant A-sites being intermediate ($\approx 2.47 \text{ \AA}$). This difference arises from octahedral distortions rather than from distinct octahedral rotations around the two species. For $x = 0.2$, the A-site cages on average are larger than those for $x = 0.1$ but the differences between the chemically distinct types are strongly diminished (Na, 2.57 \AA ; \square – 2.54 \AA ; Bi, 2.54 \AA); the

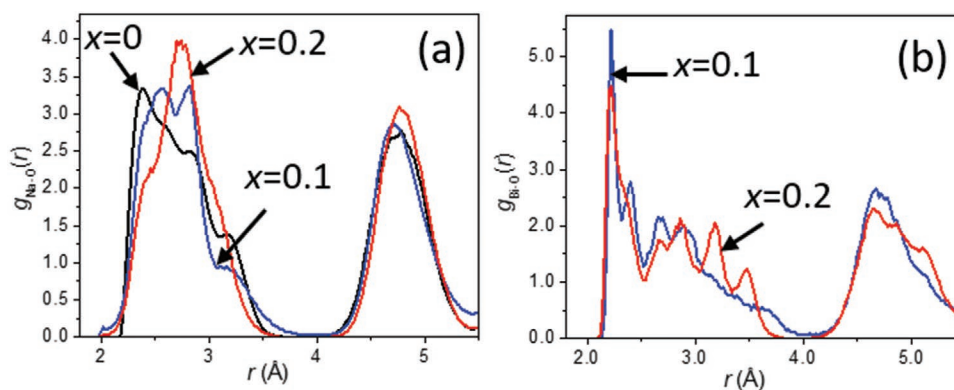


Figure 9. Nearest-neighbor a) Na–O and b) Bi–O distance distributions as obtained from the atomic configurations for $x = 0.1$ (blue) and $x = 0.2$ (red) refined using the RMC method. The Na–O distances for NaNbO_3 are shown for comparison (black trace).

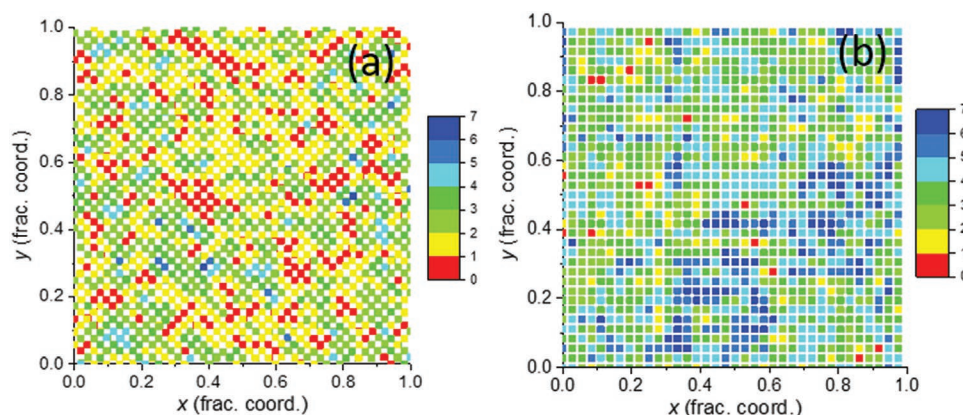


Figure 10. Maps of a single layer of $[\text{NbO}_6]$ octahedra, with each pixel representing an octahedron and the color scale reflecting the number of the A-site vacancies, n , in each associated $[\text{Nb}(\square_n(\text{Bi,Na})_{8-n})]$ cluster for a) $x = 0.1$ and b) $x = 0.2$. Clustering of octahedra with similar n values is evident. The unit cells in the two configurations are related by a 45° rotation of the crystal axes.

larger sizes of the filled A-sites are consistent with the reduced magnitudes of octahedral rotations. In the untilted A-site-ordered structure, like $\text{Bi}_{1/3}\text{NbO}_3$, the unfilled cubooctahedral cages expand as oxygen atoms shift away from the vacant A-site layers. However, in the structures of the solid-solutions, we do not observe a clear correlation between the sizes of A-site cages as defined by oxygen atoms and ionic radii of the A-site cations.

3.3. Dielectric Properties

The temperature dependence of the dielectric constant, $\epsilon(T)$, for the $\text{Na}_{1-3x}\text{Bi}_x\text{NbO}_3$ series is summarized in **Figure 14**. For $x = 0.1$, a broad peak exhibiting frequency dispersion is observed with a maximum near $T = 0^\circ\text{C}$. For larger x -values, the dependence flattens so that for $x = 0.2$, the dielectric constant of ≈ 600 varies by only $\approx 10\%$ over a temperature range from -55°C to 125°C . Weak hysteresis effects were observed for $\epsilon(T)$ measured on heating and cooling, but only at higher temperatures. The dielectric losses around room temperature were lowest for $x = 0.15$. Further analyses of the dielectric data indicated that the frequency dispersion of the dielectric constant and the increase in losses at the higher temperatures in **Figure 14** are associated with conductivity (space charge) effects.^[38] For all samples, there is weak relaxor-type behavior at lower temperatures that is presumably linked to dynamics of the local electric dipoles (but is not the primary cause of the flattening of the dielectric constant.)

Impedance spectroscopy measurements were performed for $x = 0.20$ to further clarify the nature of the observed temperature dependence of the dielectric constant. A typical complex impedance plane, Z^* , plot at 200°C (**Figure S7**, Supporting Information) exhibits a single arc. The data can be described satisfactorily (fitting error $< 2\%$) by an equivalent circuit of a single parallel resistor-constant phase element (R-CPE, inset in **Figure S7** in the Supporting Information). The impedance of a CPE can be described as $Z = [Q(j\omega)n]^{-1}$, where Q and n are the CPE parameters and ω is the frequency. The fitted value of n was close to 1, indicating a nearly ideal capacitive response. The capacitance, C , calculated^[39] from the fitted values of Q and n as $C = R((1-n)/n) \cdot Q^{(1/n)}$ was 61.35 pS cm^{-1} , which corresponds

to a permittivity of ≈ 650 , in close agreement with the value determined from the LCR measurements. The impedance data are consistent with the sample being electrically homogeneous with a single-mode bulk response. By contrast, a core-shell microstructure, would result in an inhomogeneous electrical structure, yielding either a highly distorted arc or several overlapping arcs. We therefore conclude that the flat temperature dependence of the dielectric constant for this composition reflects the intrinsic material property.

4. Discussion

Approximately similar distributions of Bi–O bond distances in the structures of $\text{Na}_{1-3x}\text{Bi}_x\text{NbO}_3$ for $x = 0.1$ and $x = 0.2$ are achieved through different displacement mechanisms. For $x = 0.1$, octahedral rotations and Bi displacements, both long-range ordered, contribute significantly to satisfying the bonding requirements of Bi. For $x = 0.2$, the dominant contribution is from (disordered) Bi off-center displacements. This order/disorder transition for Bi is linked to the distinct octahedral tilting systems in the two structures. By symmetry,^[27] in-phase octahedral rotations induce no cation displacements. Out-of-phase rotations, however, are stronger coupled to both A- and B-cation displacements and, if occurring about at least two cubic axes, or if combined with in-phase tilting, support the cooperative off-centering of cations in antiparallel patterns (the only exception is the $a^-a^-a^-$ tilt system with equal magnitudes of rotations about all three axes).

In the absence of octahedral tilting, as in the high-temperature cubic phase, relatively small Bi ions are expectedly off-centered, as indeed observed in other systems.^[7] These local shifts are disordered, with split-site/hollow Bi PDDs. A similar effect exists for Nb which is known to be locally off-centered in the cubic phases of alkaline niobates.^[30,31] As mentioned in the Introduction, octahedral rotations mitigate the underbonding of Bi and thus are expected to couple to its displacements. For $x = 0.1$, which exhibits both in-phase and out-of-phase tilts, the coupling is relatively strong and supports antiparallel ordering of both Bi and Nb displacements. In contrast, for $x = 0.2$, the

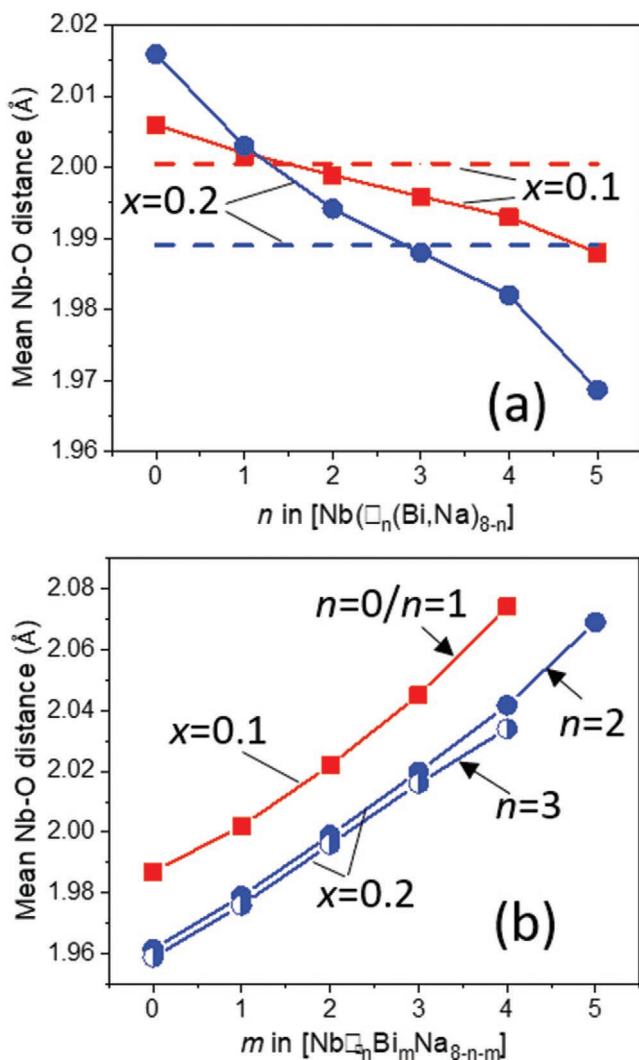


Figure 11. a) Mean Nb–O distances for individual $[\text{NbO}_6]$ octahedra as a function of the number of A-site vacancies (\square), n , in their $[\text{Nb}(\square_n(\text{Bi},\text{Na})_{8-n})]$ clusters for $x = 0.1$ (red) and $x = 0.2$ (blue). The horizontal dashed lines represent these distances as calculated from the average atomic coordinates in the crystallographic unit cell. b) Mean Nb–O distances for individual $[\text{NbO}_6]$ octahedra as a function of the number of Bi atoms, m , in $[\text{Nb}(\square_n\text{Bi}_m\text{Na}_{8-n-m})]$ for $x = 0.1$, with $n = 0/n = 1$ (squares/red), and $x = 0.2$, with $n = 2$ (solid circles) and $n = 3$ (half-filled circles). The consistency in the trends reflects the insignificance of statistical uncertainties associated with each datapoint.

predominantly in-phase tilting (of smaller magnitude compared to $x = 0.1$) only weakly affects the cations, and therefore their displacements remain disordered. These arguments apply to other Bi-based perovskite solid solutions, such as $\text{Na}_{1/2}\text{Bi}_{1/2}\text{TiO}_3\text{-K}_{1/2}\text{Bi}_{1/2}\text{TiO}_3$,^[37] for which distinct coupling between displacements of Bi and in-phase versus out-of-phase octahedral rotations explains the anomalous behavior of the Curie temperature.

The order/disorder transition for the cation displacements appears to manifest in the dielectric properties of $\text{Na}_{1-3x}\text{Bi}_x\text{NbO}_3$. Overall, the trends observed in $\epsilon(T)$ are similar to those reported for the $\text{NaNbO}_3\text{-Gd}_{1/3}\text{NbO}_3$ ^[40] and $\text{AgNbO}_3\text{-Bi}_{1/3}\text{NbO}_3$ ^[12] systems. These types of solid solutions which

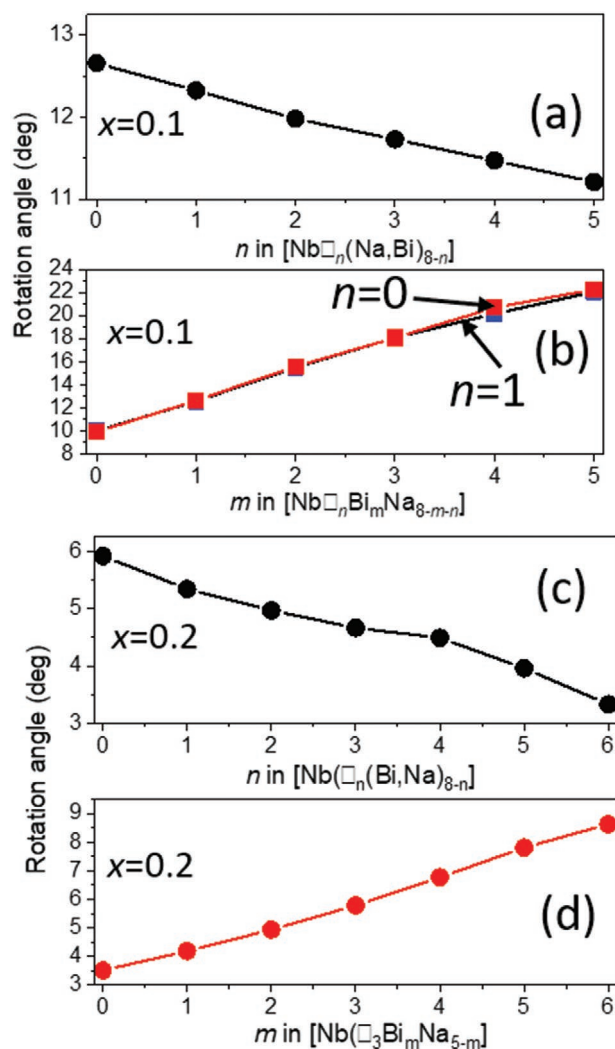


Figure 12. Rotation angle for $[\text{NbO}_6]$ octahedra in a) $x = 0.1$ and c) $x = 0.2$ as a function of the number of A-site vacancies (\square), n , in the $[\text{Nb}(\square_n(\text{Bi},\text{Na})_{8-n})]$ clusters. Rotation angle as a function of the number of Bi atoms, m , in $[\text{Nb}(\square_n\text{Bi}_m\text{Na}_{8-n-m})]$ clusters with fixed n -values for b) $x = 0.1$ and d) $x = 0.2$.

include an antiferroelectric-like end member are characterized by an abrupt decrease in the temperature of maximum permittivity and a dramatic flattening of $\epsilon(T)$ above a certain fraction of the second component^[40] (in the present case, the threshold is near $x = 0.1$). As in $\text{Na}_{1-3x}\text{Bi}_x\text{NbO}_3$, the $\text{Ag}_{1-3x}\text{Bi}_x\text{NbO}_3$ system apparently exhibits a preference for in-phase octahedral rotations with increasing x . While no structural information could be found for $\text{NaNbO}_3\text{-Gd}_{1/3}\text{NbO}_3$ solid solutions, its displacive behavior is likely to resemble that of the Bi-substituted systems: the ionic radius of Gd^{3+} in 12-fold coordination is projected to be 1.28 \AA , which predicts local off-centering of these cations on the A-sites. We propose that the flattening of $\epsilon(T)$ is primarily caused by the nanoscale modulations of lattice distortions, combined with the liberation of cation-displacement ordering when out-of-phase rotations vanish. Other types of NaNbO_3 -based solid solutions which combine several B-cations, such as $\text{Na}(\text{Nb},\text{Ta})\text{O}_3$, also exhibit strong broadening of $\epsilon(T)$ beyond a

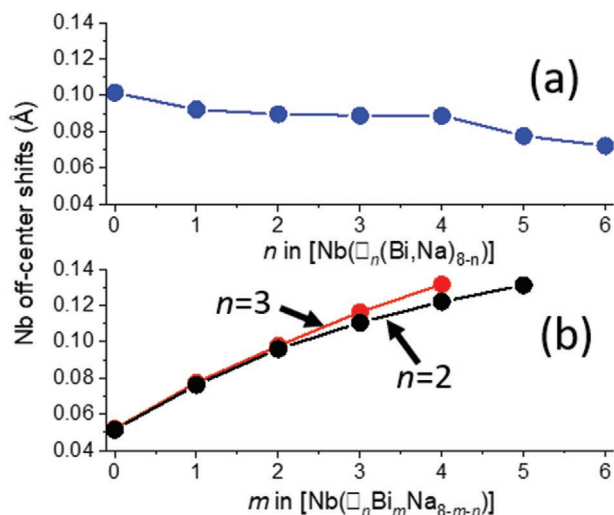


Figure 13. Magnitudes of Nb displacements off octahedral centers for $x = 0.2$ as a function of n and m in the a) $[\text{Nb}\square_n(\text{Bi,Na})_{8-n}]$ and b) $[\text{Nb}\square_n\text{Bi}_m\text{Na}_{8-m-n}]$ clusters, respectively. In (b), the results for $n = 2$ and $n = 3$ are shown using black and red colors, respectively.

certain (in this case Ta) concentration;^[40] however, the underlying structural mechanism in such B-site-substituted systems is different, resembling that proposed for $\text{Ag}(\text{Nb,Ta})\text{O}_3$.^[41]

5. Conclusions

Bismuth substitution for sodium according to the formula $\text{Na}_{1-3x}\text{Bi}_x\text{NbO}_3$ yields a single perovskite-like phase for $x \leq 0.2$. Long-range ordering of octahedral rotations is suppressed as x increases; for out-of-phase tilts it is absent for $x > 0.1$, and for in-phase tilts, limited to the nanoscale at $x = 0.2$. The disappearance of ordered out-of-phase rotations coincides with an order–disorder transition in the displacements of Bi and Nb, as indicated by transformations of their respective probability density distributions from unimodal to multisite/hollow. This abrupt change in the cation behavior ensues from different strengths of coupling with out-of-phase (strong) versus in-phase (weak) rotations, and is driven primarily by the relatively covalent bonding requirements of Bi^{3+} ions. In the absence of octahedral rotations, Bi cations on the Na sites, with their lone pairs of electrons, are expected to be displaced from the centers of the cuboctahedra, as observed, for example, in $\text{Bi}_{1/3}\text{NbO}_3$ ($x = 1/3$). Long-range ordering of out-of-phase rotations, if present, couples strongly to the local displacements of Bi and Nb, thereby promoting their ordering. Otherwise, these displacements remain disordered. Charge-compensation dictates that for each Bi that substitutes for Na in $\text{Na}_{1-3x}\text{Bi}_x\text{NbO}_3$, two A-site vacancies must form; therefore, the undercoordination of oxygen increases markedly with the x -value. The structural relaxations which occur to mitigate this underbonding result in nanoscale modulations of the lattice distortions. We suggest these modulations and the onset of the Bi and Nb displacive disorder are primarily responsible for the flattening of the temperature dependence of the dielectric constant. Because each A-cation (or vacancy) affects the distortions of eight octahedra

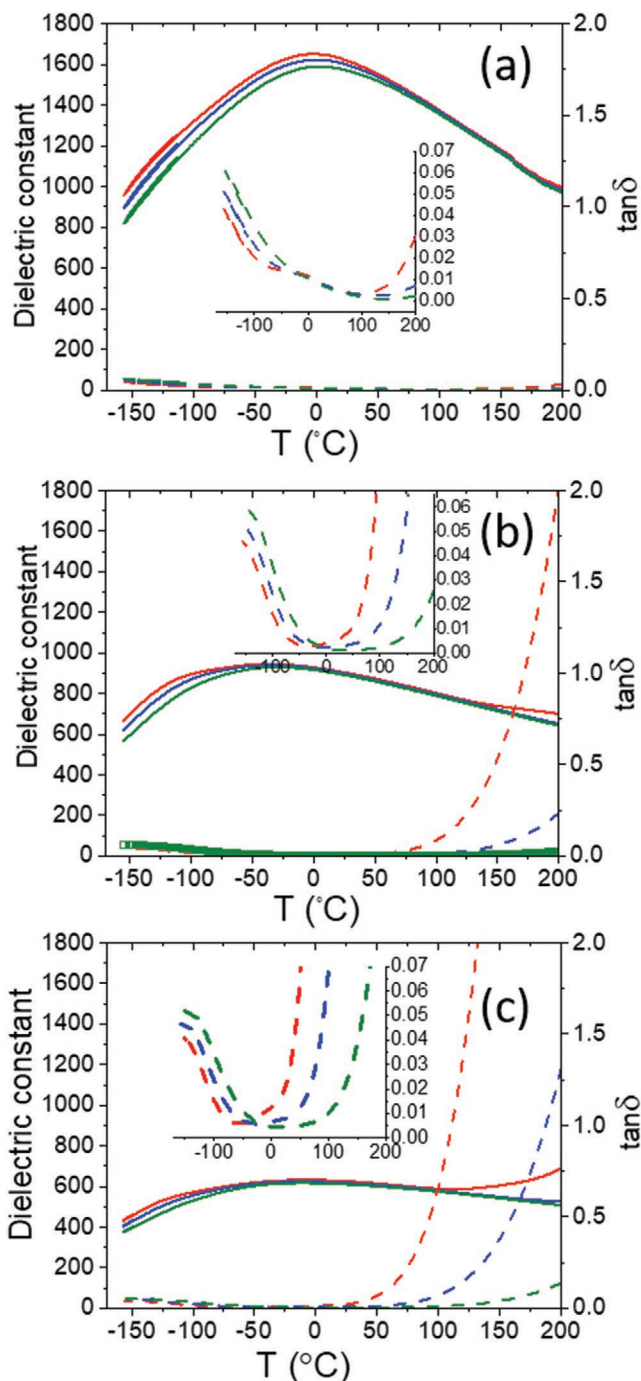


Figure 14. Dielectric constant and loss ($\tan\delta$) versus temperature for a) $x = 0.1$, b) $x = 0.15$, and c) $x = 0.2$. Insets display magnifications of the $\tan\delta$ behavior.

in adjacent unit cells, even dilute A-site substitutions can have significant effects on the dielectric and ferroelectric properties.

Supporting Information

Supporting Information is available from the Wiley Online Library or from the author.

Acknowledgements

A computer script for building models with ordered nanodomains was written by M. Eremenko. Stimulating discussions with T. Vanderah and V. Krayzman are acknowledged. Diamond Light Source is thanked for access to beamlines I15-1 and B18 and EPSRC (F.Y., D.C.S.) for funding (EP/L027348/1).

Conflict of Interest

The authors declare no conflict of interest.

Keywords

dielectric, disorder, pair distribution functions, perovskites, solid solutions, X-ray scattering

Received: February 26, 2020

Revised: March 27, 2020

Published online: June 4, 2020

- [1] T. Takenaka, K. Maruyama, K. Sakata, *Jpn. J. Appl. Phys.* **1991**, *30*, 2236.
- [2] J. Rodel, J. F. Li, *MRS Bull.* **2018**, *43*, 576.
- [3] M. A. Beuerlein, N. Kumar, T. M. Usher, H. J. Brown-Shaklee, N. Raengthon, I. M. Reaney, D. P. Cann, J. L. Jones, G. L. Brennecke, *J. Am. Ceram. Soc.* **2016**, *99*, 2849.
- [4] M. Li, M. J. Pietrowski, R. A. De Souza, H. R. Zhang, I. M. Reaney, S. N. Cook, J. A. Kilner, D. C. Sinclair, *Nat. Mater.* **2014**, *13*, 31.
- [5] R. Seshadri, N. A. Hill, *Chem. Mater.* **2001**, *13*, 2892.
- [6] V. M. Goldsmith, *Naturwissenschaften* **1926**, *14*, 477.
- [7] I. Levin, D. S. Keeble, G. Cibir, H. Y. Playford, M. Eremenko, V. Krayzman, W. J. Laws, I. M. Reaney, *Chem. Mater.* **2019**, *31*, 2450.
- [8] I. Levin, V. Krayzman, J. C. Woicik, F. Bridges, G. E. Sterbinsky, T. M. Usher, J. L. Jones, D. Torrejon, *Phys. Rev. B* **2016**, *93*, 104106.
- [9] D. S. Keeble, E. R. Barney, D. A. Keen, M. G. Tucker, J. Kreisel, P. A. Thomas, *Adv. Funct. Mater.* **2013**, *23*, 185.
- [10] E. Aksel, J. S. Forrester, J. C. Nino, K. Page, D. P. Shoemaker, J. L. Jones, *Phys. Rev. B* **2013**, *87*, 104113.
- [11] I. Levin, I. M. Reaney, *Adv. Funct. Mater.* **2012**, *22*, 3445.
- [12] X. Hu, M. Valant, D. Suvorov, *J. Appl. Phys.* **2006**, *99*, 124109.
- [13] A. M. Glazer, K. Ishida, *Ferroelectrics* **1973**, *6*, 219.
- [14] K. Ishida, A. M. Glazer, *Ferroelectrics* **1973**, *6*, 293.
- [15] K. E. Johnston, C. C. Tang, J. E. Parker, K. S. Knight, P. Lightfoot, S. E. Ashbrook, *J. Am. Chem. Soc.* **2010**, *132*, 8732.
- [16] R. D. Shannon, *Acta Crystallogr. A* **1976**, *32*, 751.
- [17] W. G. Mumme, I. E. Grey, B. Edwards, C. Turner, J. C. Nino, T. A. Vanderah, *J. Solid State Chem.* **2013**, *200*, 323.
- [18] M. Basham, J. Filik, M. T. Wharmby, P. C. Y. Chang, B. El Kassaby, M. Gerring, J. Aishima, K. Levik, B. C. Pulford, A. Sikharulidze, I. Sneddon, D. Webber, M. Dhesi, S. S. Maccherozzi, F. O. Svensson, S. Brockhauser, G. Naray, A. W. Ashtona, *J. Synchrotron Radiat.* **2015**, *22*, 853.
- [19] P. Juhas, T. Davis, C. L. Farrow, S. J. L. Billinge, *J. Appl. Crystallogr.* **2013**, *46*, 560.
- [20] B. Ravel, M. Newville, *J. Synchrotron Radiat.* **2005**, *12*, 537.
- [21] J. J. Rehr, J. J. Kas, M. P. Prange, A. P. Sorini, Y. Takimoto, F. Vila, C. R. Phys. **2009**, *10*, 548.
- [22] A. A. Coelho, *J. Appl. Crystallogr.* **2018**, *51*, 210.
- [23] The identification of any commercial product or trade name does not imply endorsement or recommendation by the National Institute of Standards and Technology.
- [24] M. G. Tucker, D. A. Keen, M. T. Dove, A. L. Goodwin, Q. Hui, *J. Phys.: Condens. Matter* **2007**, *19*, 335218.
- [25] V. Krayzman, I. Levin, J. C. Woicik, T. Proffen, T. A. Vanderah, M. G. Tucker, *J. Appl. Crystallogr.* **2009**, *42*, 867.
- [26] M. Eremenko, V. Krayzman, A. Gagin, I. Levin, *J. Appl. Crystallogr.* **2017**, *50*, 1561.
- [27] A. M. Glazer, *Acta Crystallogr., Sect. B: Struct. Crystallogr. Cryst. Chem.* **1972**, *28*, 3384.
- [28] M. D. Peel, S. P. Thompson, A. Daoud-Aladine, S. E. Ashbrook, P. Lightfoot, *Inorg. Chem.* **2012**, *51*, 6876.
- [29] I. D. Brown, D. Altermatt, *Acta Crystallogr., Sect. B: Struct. Sci.* **1985**, *41*, 244.
- [30] V. A. Shuvaeva, A. Azuma, K. Yagi, K. Sakaue, H. Terauchi, *J. Synchrotron Radiat.* **2001**, *8*, 833.
- [31] V. A. Shuvaeva, K. Yanagi, K. Y., K. Sakaue, H. Terauchi, *Solid State Commun.* **1998**, *106*, 335.
- [32] I. Levin, V. Krayzman, J. C. Woicik, *Appl. Phys. Lett.* **2013**, *102*, 162906.
- [33] P. M. Woodward, *Acta Crystallogr., Sect. B: Struct. Sci.* **1997**, *53*, 44.
- [34] P. M. Woodward, A. W. Sleight, T. Vogt, *J. Solid State Chem.* **1997**, *131*, 9.
- [35] E. E. Rodriguez, A. Llobet, T. Proffen, B. C. Melot, R. Seshadri, P. B. Littlewood, A. K. Cheetham, *J. Appl. Phys.* **2009**, *105*, 114901.
- [36] C. J. Howard, G. R. Lumpkin, R. I. Smith, Z. M. Zang, *J. Solid State Chem.* **2004**, *177*, 2726.
- [37] I. Levin, I. M. Reaney, E. M. Anton, W. Jo, J. Rodel, J. Pokorny, L. A. Schmitt, H. J. Kleebe, M. Hinterstein, J. L. Jones, *Phys. Rev. B* **2013**, *87*, 024113.
- [38] A. K. Jonscher, *J. Mater. Sci.* **1981**, *16*, 2037.
- [39] J. Fleig, *Solid State Ionics* **2002**, *150*, 181.
- [40] I. P. Raevski, S. A. Prosandeev, *J. Phys. Chem. Solids* **2002**, *63*, 1939.
- [41] I. Levin, J. C. Woicik, A. Llobet, M. G. Tucker, V. Krayzman, J. Pokorny, I. M. Reaney, *Chem. Mater.* **2010**, *22*, 4987.